Validation of contact mechanics models for Atomic Force Microscopy via Finite Elements Analysis and nanoindentation experiments

L. Dal Fabbro, H. Holuigue[1], M. Chighizola[2,]* and A. Podestà*

Dipartimento di Fisica "Aldo Pontremoli", Università degli Studi di Milano, via G. Celoria 16, 20133, Milano, Italy.

CIMaINa, Università degli Studi di Milano, via G. Celoria 16, 20133, Milano, Italy.

*Corresponding authors. E-mail: matteo.chighizola@inserm.fr, alessandro.podesta@unimi.it

SUPPLEMENTARY INFORMATION

[1] Present affiliation: Mechanobiology Institute (MBI), National University of Singapore, 5A Engineering Drive 1, 117411, Singapore
[2] Present affiliation: Institut national de la santé et de la recherche médicale (INSERM), Dynamo Group, 163 avenue de Luminy, Marseille, France.

Table of Contents

Note S1. Contact radius of a spherical tip affected by large indentations

In the work of Kontomaris *et. al.*[1] it is explicitly reported an expression for the corrected contact radius a when the spherical tip of radius R can no longer be approximated by a paraboloid:

$$\frac{a}{R} = c_1\gamma^{1/2} + c_2\gamma + c_3\gamma^2 + c_4\gamma^3 + c_5\gamma^4 + c_6\gamma^5 \quad \text{(S0)}$$

, being $\gamma = \delta/R$. The coefficients c_k are reported in the main text (see Eq. 6).

On the other hand, Muller *et. al.*[2] do not present any formula for the contact radius in the p. We therefore explicitly computed the Muller's contact radius on the basis of his large indentations corrective factor $\Omega_M(\gamma)$.

We took advantage of the general relationship linking the contact radius a, the deformation δ and the applied force F by an axisymmetric body indenting an elastic half space with Young's modulus E and Poisson's ratio ν:[3]

$$\frac{dF}{d\delta} = \frac{2E}{1-\nu^2}a \quad \text{(S1)}$$

When the large indentations effect is present, the applied force F can be written as

$$F = F_H(\delta) \cdot \Omega_M(\delta/R) \quad \text{(S2)}$$

, being $F_H(\delta)$ the equivalent Hertzian force, valid for a paraboloidal indenter.

Inserting Eq. S2 into Eq. S1 and noting that $d\Omega_M/d\gamma \approx -0.1$ when $\gamma \in [0,1]$, it follows:

$$a \approx \Omega_M a_H - 0.1\frac{2}{3}\frac{\delta^{3/2}}{\sqrt{R}} \approx a_H(\Omega_M - 0.07\gamma) \quad \text{(S3)}$$

, where $a_H = \sqrt{R\delta}$ is the Hertzian contact radius. The corrective factor within round brackets in Eq. S3 depends only on the nondimensional ratio γ.

Note S2. Garcia's bottom effect correction for an arbitrary Poisson's ratio and the formulae for the contact radius accounting for the bottom effect

Garcia's bottom effect correction for an arbitrary Poisson's ratio

Within the framework of linear elasticity proposed by Garcia *et al.,* we solved Eq. S21 in the Supporting Information of Ref.[4], using a custom routine based on the Symbolic Math Toolbox of MATLAB (Mathworks). We obtained the expression of the corrective factor Δ_G for the bonded case for an arbitrary value of the Poisson's ratio up to the desired order in χ. The corrective factor of Garcia Δ_G, up to the fifth order, is:

$$\Delta_G = 1 + A\chi + B\chi^2 + C\chi^3 + D\chi^4 + E\chi^5 \tag{S4}$$

, where the coefficients are:

$$A = \frac{2\alpha_0}{\pi}$$

$$B \approx \frac{301\pi\alpha_0^2}{2000}$$

$$C \approx -\pi\left(\frac{31\alpha_0^3}{255} + \frac{106\beta_0}{491}\right)$$

$$D \approx \pi\left(\frac{24\alpha_0^4}{245} + \frac{40\beta_0\alpha_0}{97}\right)$$

$$E \approx -\pi\left(\frac{\alpha_0^5}{22} + \frac{2\beta_0\alpha_0^2}{9}\right)$$

, with:

$$\alpha_0 = -\frac{1.2876 - 1.4678\nu + 1.3442\nu^2}{1-\nu}$$

$$\beta_0 = \frac{0.6387 - 1.0277\nu + 1.5164\nu^2}{1-\nu}$$

The quantities α_0 and β_0 are defined as in Dimitriadis *et al.*[5] for the bonded case. The given expression of the coefficient A is analytically exact, whereas the ones of B, C, D and E well approximate the true values up to the 4th decimal point. The fifth-order term in Eq. S4 does not contribute significantly to the evaluation of the Young's modulus (less than 0.3%), hence we have used the expression of Δ_G truncated to the fourth order (Eq. 12b in the main text).

Garcia's contact radius expansion up to the 5th order in χ

In Garcia *et al.* the contact radius is evaluated as (Eq, S23 in the Supporting Information of Ref. [4]):

$$a_G = \sqrt{\delta R} - \frac{2\alpha_0 R\delta}{3h\pi} = a_H(1 + p_1\chi) \tag{S5}$$

, obtained through the minimization of the derivative of the first two terms of the force with respect to the contact radius (see Eq. S21-S22 in the SI of Ref. [4]); a_H is the Hertzian contact radius, $\chi = \sqrt{R\delta}/h$ and $p_1 = -(2\alpha_0/3\pi)$. The corrective factor within round brackets in Eq. S5 depends only on the nondimensional ratio χ.

In this work, we evaluated the expression of the contact radius within the framework of Garcia by performing the minimization of the derivative of the complete force expression provided in Eq. S21 of Ref.[4]. We found that also when considering the full force expression, the contact radius may be expressed as the Hertzian contact radius multiplied by a polynomial expansion in χ. The expansion of the Garcia's contact radius (bonded case) up to the 5th order, for an arbitrary Poisson's ratio ν, is:

$$a_G^{\text{full\_exp}} = a_H(1 + p_1\chi + p_2\chi^2 + p_3\chi^3 + p_4\chi^4 + p_5\chi^5) \tag{S6}$$

, with coefficients p_i depending solely upon α_0 and β_0 :

$$p_1 = -\frac{2\alpha_0}{3\pi} = -0.2122\ \alpha_0$$

$$p_2 = 0.1126\ \alpha_0^2$$

$$p_3 = -(0.0765\ \alpha_0^3 + 0.5093\ \beta_0)$$

$$p_4 = 0.0585\ \alpha_0^4 + 0.5764\ \alpha_0\beta_0$$

$$p_5 = 0.1261\ \alpha_0^5 + 0.9250\ \alpha_0^2\beta_0$$

The coefficients were determined using a custom routine based on the Symbolic Math Toolbox of MATLAB (Mathworks). Also, in this case, the corrective factor in Eq. S6 depends only on the nondimensional ratio χ.

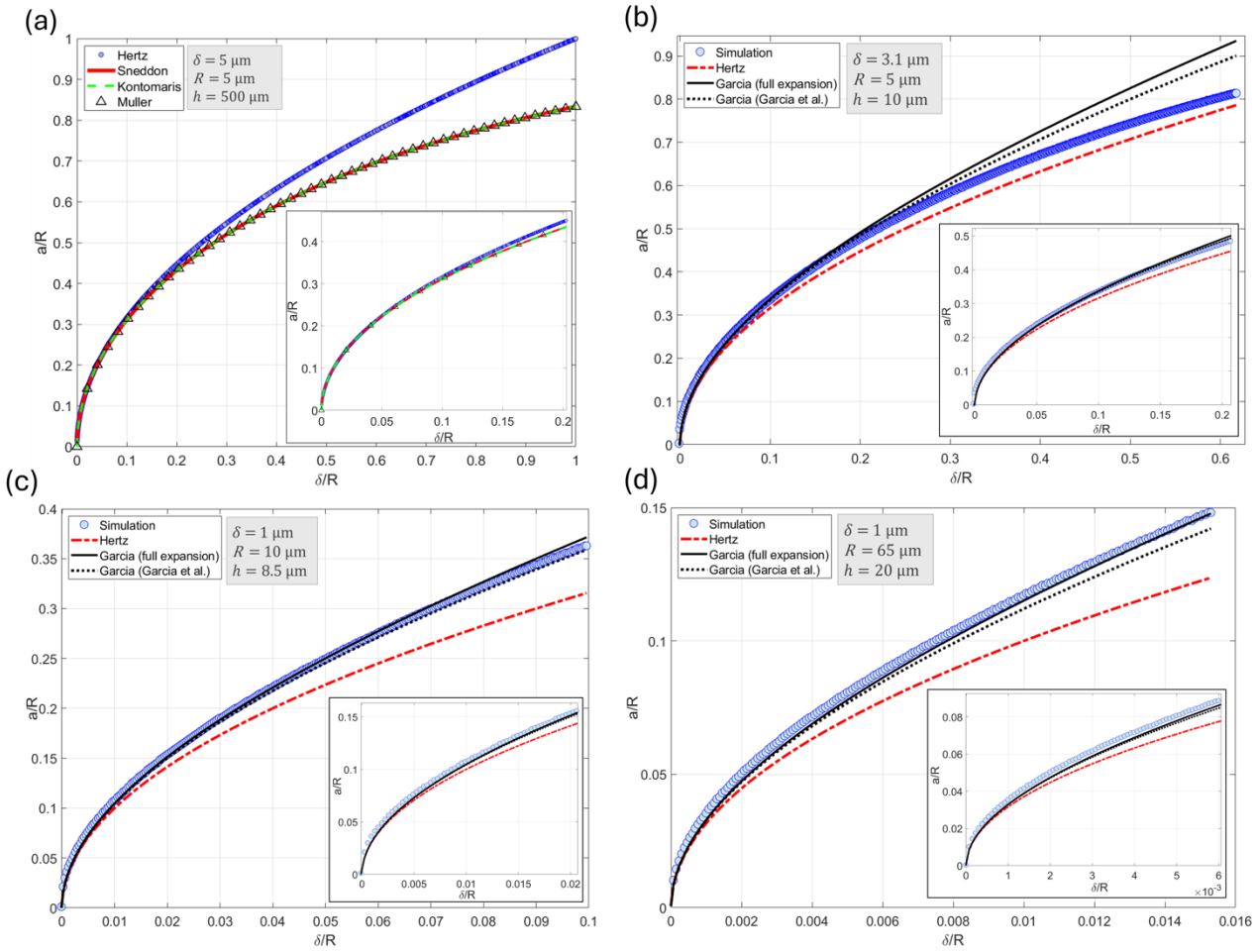

Figure S1. Evolution of the reduced contact radius a/R with the δ/R ratio for different simulated systems (bulk and thin films, spherical indenter) based on different contact mechanics models (Hertz and Sneddon models; Hertz + $LIC_{M/K}$ models; Hertz + BEC_G models). The insets show an expanded view of the small δ/R values region. (a) Bulk systems. The contact radius including Muller's large indentation correction was calculated using Eq. S3 (see Note S1), whereas the radius including Kontomaris' correction is taken from Eq. 8 of Ref.[1]. The Sneddon radius is obtained from Eq. 4 in the main text. (b-d) Thin-Film systems, spherical indenter, different combinations of parameters δ, R and h leading to the same $\chi = 0.4$ (see Table 1 in the main text). The contact radius including Garcia's bottom effect correction up to the 1st order in χ was taken from Ref. [4] (Eq. S5 above), while the radius including Garcia's bottom effect correction up to the 5th order was calculated using Eq. S6 (see Note S2).

In bulk systems (a), the radii obtained using both Muller's and Kontomaris' large indentation corrections provide excellent agreement with the simulated data, as well as with the Sneddon model for the spherical indenter. In the thin film condition (b-d), the radii obtained using Garcia's bottom effect correction perform better than the Hertzian radius, as long as the large indentation effect is weak (i.e. for small δ/R values, compare (c,d) to (b)).

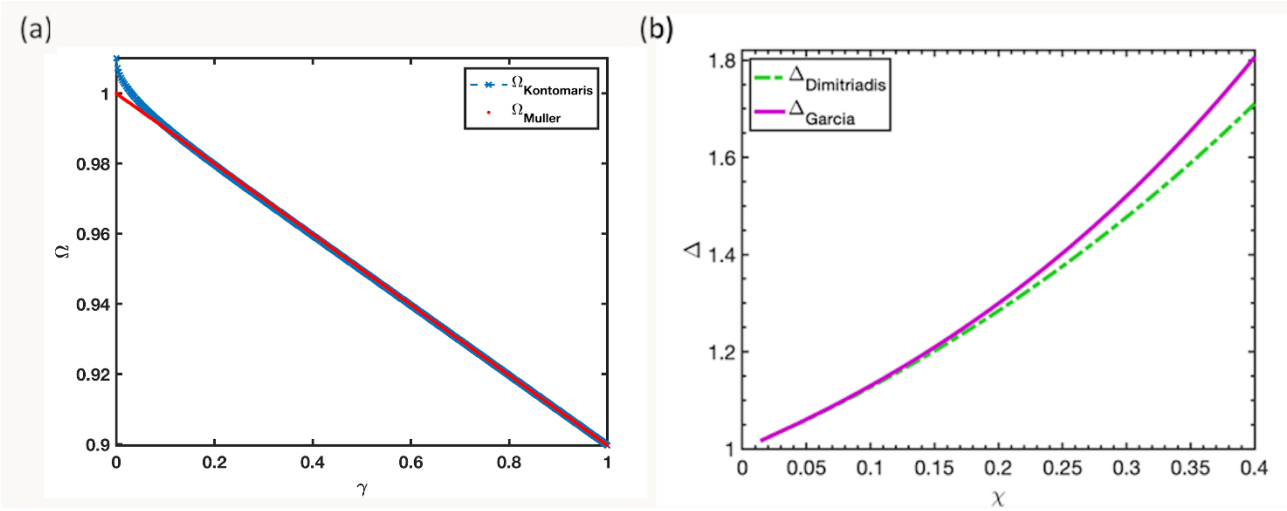

Figure S2. The correction functions $\Omega(\gamma)$ and $\Delta(\chi)$ for the Hertz model ($\gamma = \delta/R$, $\chi = a_{Hertz}/h = \sqrt{R\delta}/h$, $\nu = 0.5$) for a bonded sample in the explored ranges of the parameters: (**a**) LIC; (**b**) BEC.

Note S3. Linearity of Tabor and Kalidindi effective stress on strain

Tabor defined effective stress σ^* and strain ε^* as[6]

$$\varepsilon^* = 0.2\frac{a}{R} = 0.2\frac{\delta}{a} \tag{S7}$$

$$\sigma^* = \frac{F}{\pi a^2} \tag{S8}$$

, where $a = \sqrt{R\delta}$ is the Hertzian contact radius and F is the applied force, υ is the Poisson's ratio and E is the Young's modulus. The prefactor 0.2 was empirically determined by Tabor [6]. At odd with the case of equivalent von Mises stress and strain, which are local quantities, Tabor stress and strain form a single pair of values representing the elastic response of the system as a whole. For a linear elastic material obeying Hertzian mechanics, it follows:

$$\sigma^* = \frac{20}{3\pi}\frac{E}{(1-\upsilon^2)}\varepsilon^* \tag{S9}$$

Kalidindi *et al.*[7] proposed an alternative definition of effective stress and strain:

$$\varepsilon^* = \frac{4}{3\pi}\frac{\delta}{a} \tag{S10}$$

$$\sigma^* = \frac{F}{\pi a^2} \tag{S11}$$

, from which it follows:

$$\sigma^* = \frac{E}{1-\upsilon^2}\varepsilon^* \tag{S12}$$

The effective Kalidindi's strain is approximately twice the one predicted by Tabor's formula; apart from a numerical factor, the scaling of the two stress-strain pairs is the same.

Note S4. Linearity of equivalent von Mises stress on strain

In each simulation, a strain and stress field developes inside the deformed material. From the stress field, a scalar representing a pointwise stress state, called the equivalent (von Mises) stress field σ_{equiv}, may be computed. Similarly, the equivalent strain $\varepsilon_{\text{equiv}}$ exist. These two quantities are defined as below:

$$\sigma_{\text{equiv}} = \sqrt{\frac{(\sigma_1-\sigma_2)^2+(\sigma_2-\sigma_3)^2+(\sigma_3-\sigma_1)^2}{2}}$$

$$\varepsilon_{\text{equiv}} = \frac{1}{1+\nu}\sqrt{\frac{(\varepsilon_1-\varepsilon_2)^2+(\varepsilon_2-\varepsilon_3)^2+(\varepsilon_3-\varepsilon_1)^2}{2}} \qquad \text{(S13)}$$

, where ν is the Poisson's ratio, σ_j and ε_j are the principal stress and strain components, respectively, i.e. the eigenvalues of the stress and strain tensor. Since σ_{equiv} and $\varepsilon_{\text{equiv}}$ are expressed in terms of the principal components, they are invariant under any change of base. For each simulation, ANSYS provides the maximum and the minimum equivalent stress and strain over time.

Starting from the generalized Hooke's law, in the regime of linear elasticity, it holds that

$$\sigma_{\text{equiv}} = E\varepsilon_{\text{equiv}}$$

where E is the Young's modulus. The demonstration follows.

The starting point is the generalized Hooke's law

$$\varepsilon_{ik} = \frac{1}{9K}\delta_{ik}\sum_l \sigma_{ll} + \frac{1}{2\mu}\left(\sigma_{ik} - \frac{1}{3}\sum_l \sigma_{ll}\right)$$

, where $\sum_l \sigma_{ll} = Tr(\sigma)$ is the trace of the stress tensor, K and μ are the uniform compression and shear modulus, respectively. By choosing a suitable base in which both ε and σ are diagonal, we compute the p-th principal value of the strain tensor (p=1,2,3) as

$$\varepsilon_p = Tr(\sigma)\left(\frac{1}{9K} - \frac{1}{6\mu}\right) + \frac{\sigma_p}{2\mu}$$

Therefore, the difference between the p-th and the b-th strain principal values reads

$$\varepsilon_p - \varepsilon_b = \frac{1}{2\mu}(\sigma_p - \sigma_b) \qquad \text{(S14)}$$

By inserting Eq. S14 in the definition of $\varepsilon_{\text{equiv}}$ (Eq. S13), one obtains:

$$\varepsilon_{\text{equiv}} = \frac{1}{2\mu(1+\nu)}\sigma_{\text{equiv}}$$

noting that, by definition:

$$\nu = \frac{1}{2}\frac{3K - 2\mu}{3K + \mu}$$

, and

$$E = \frac{3K + \mu}{9K\mu}$$

, one finds:

$$\frac{1}{2\mu(1 + \nu)} = \frac{1}{E}$$

It follows:

$$\sigma_{\text{equiv}} = E\varepsilon_{\text{equiv}} \tag{S15}$$

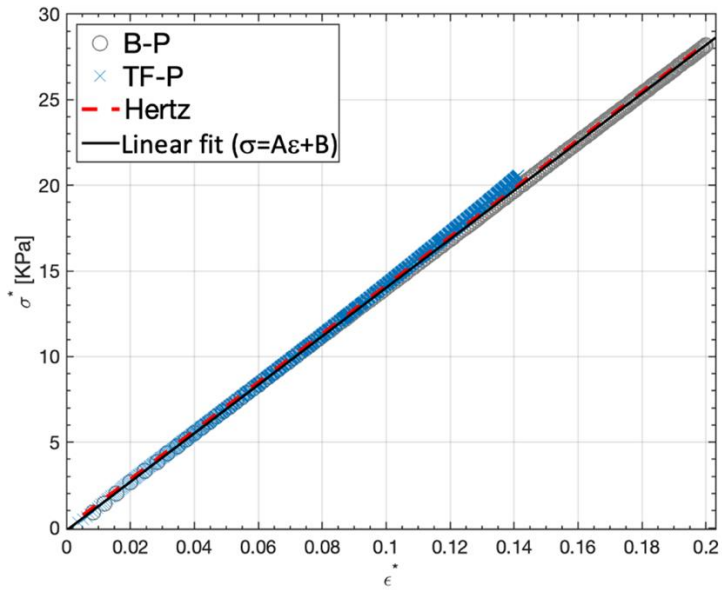

Figure S3. Tabor effective stress vs effective strain for the Bulk-Paraboloid (B-P) and Thin Film-Paraboloid (TF-P) configurations. Effective stress and strain have been calculated according to Eqs. S7, S8 (see Note S3). (o) Bulk-Paraboloid (B-P) simulated data. (**x**) Thin Film-Paraboloid (TF-P) simulated data, corrected using Garcia's formula BEC_G. (**---**) Effective stress-strain curve computed using the Hertzian contact radius. (——) Linear fit to the B-P simulated data.

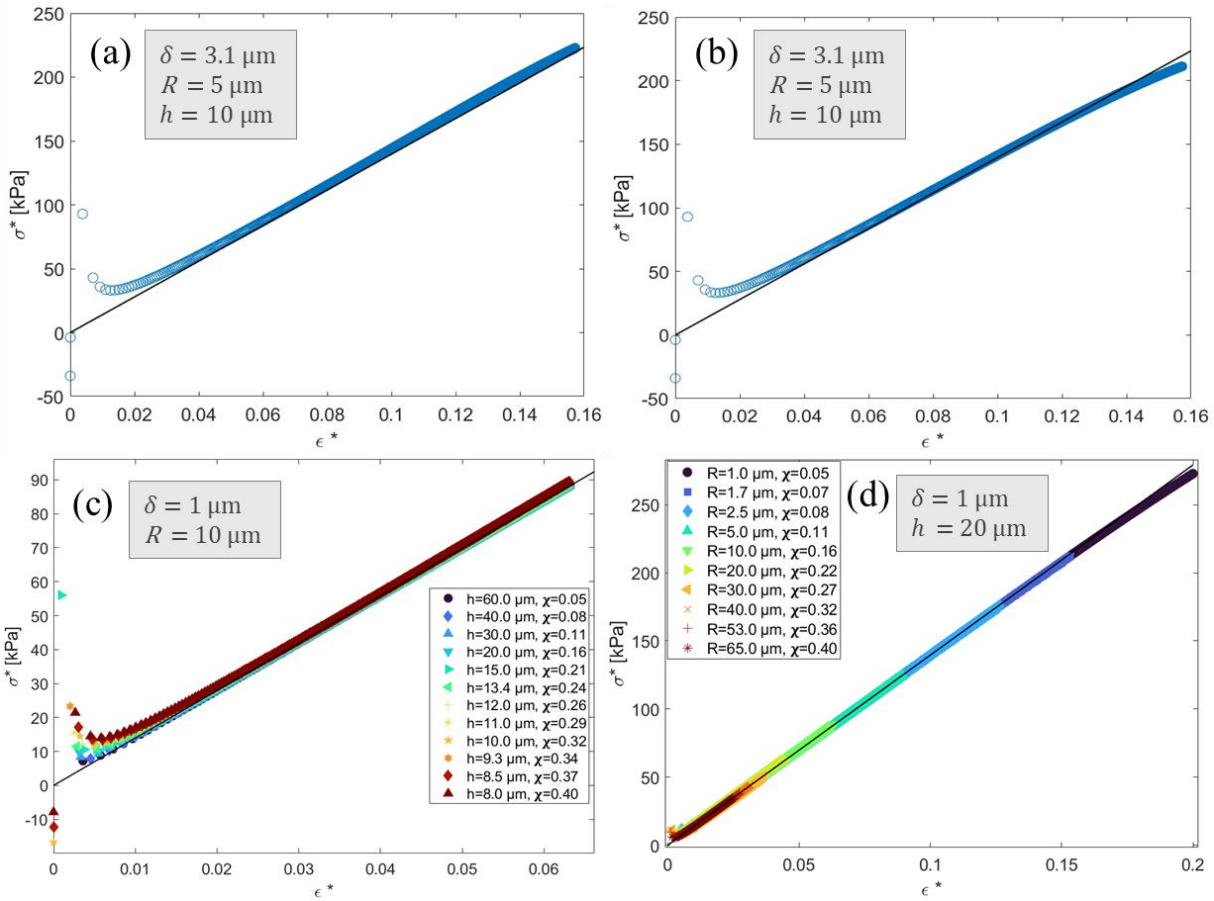

Figure S4. Effective stress vs effective strain plots of the Thin Film-Sphere (TF-S) systems (see Note S3). The effective stress and strains are computed using the Tabor[6] formulae (Eqs. S7, S8)[7] after applying BEC+LIC. At odd with the case of von Mises stress and strain (Figure S5f), which are local equivalent quantities, the effective Tabor stress and strain represent averages across the whole deformation volume, whose definition implies the specific Hertz model; the linearity of the effective stress vs effective strain relationship, therefore, must be tested after application of BEC and LIC. The force curves were corrected using Garcia's BEC and Muller's LIC, except in (a), where Dimitriadis' BEC was used, since it performs slightly better in the specific simulated conditions. (a) TF-S system corresponding to $\chi = 0.4$ corrected with Muller's LIC and Dimitriadis' BEC. (b) TF-S system corresponding to $\chi = 0.4$ corrected with Muller's LIC and Garcia's BEC. (c) TF-S systems in which the elastic medium thickness was varied. (d) TF-S systems where the tip radius was varied (see Table 1 in the main text). The solid black line represents Eq. S9, using the nominal Young's modulus of the elastic medium. The well-defined linear relations of the effective stress/strain curves confirm that in our simulations the linear elastic regime holds. The nonlinearity of the small-strain region can be attributed to the finite resolution (approx. 20-80 nm) of the simulation mesh, which affects both effective stress and strain values for $\varepsilon^* \lesssim 0.015$.

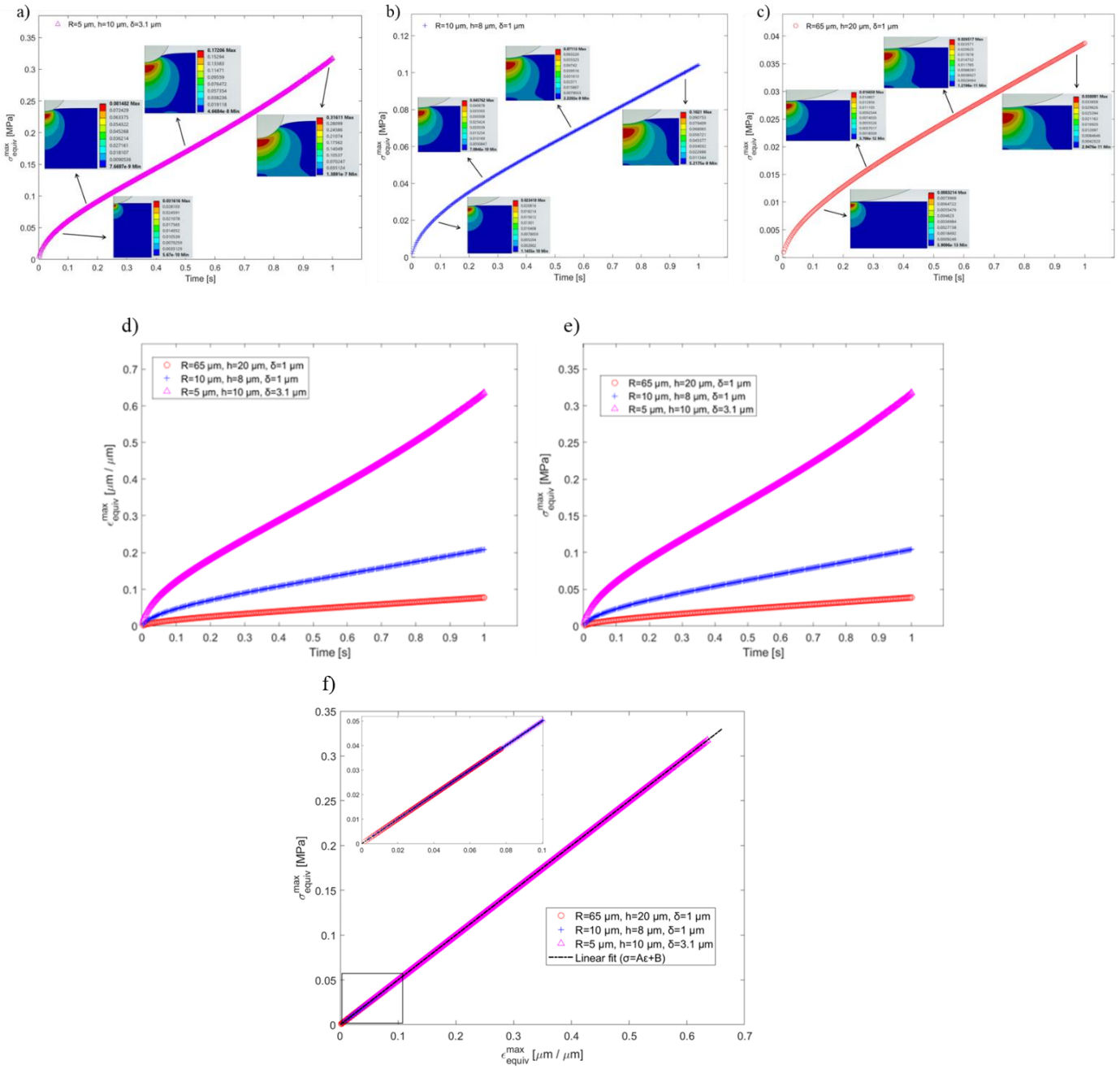

Figure S5. Maximum equivalent von Mises stress and strain for the Thin Film-Sphere (TF-S) systems. (**a-c**) Maximum equivalent von Mises' stress (see Note S4) versus fictitious time of the simulation for the three TF-S simulated systems (see Table 1 in the main text) with insets showing the geometry of the stress field developing in the elastic medium as the tip indents. The units of the insets are MPa. (**d-e**) maximum equivalent (von Mises) stress (same as in a-c) and strain of the three TS-S systems. (**f**) equivalent stress vs equivalent strain for the three TF-S systems, along with a linear fit $\sigma = A\varepsilon + B$ (black dashed line). The linear fit reproduces with excellent agreement the simulated data, providing $A = 0.5$ MPa, which is the nominal Young's modulus of the simulated material, and $B \approx 0$, as expected. It is worth stressing that the fitted equivalent stress and strain are raw data taken from the simulations, hence neither BEC nor LIC corrections were applied. These results are consistent with the fact that the linear elastic behavior holds also in confined geometries, irrespective of the boundary conditions. The fact that the curves follow a linear trend further confirms that the linear elastic regime holds in all our simulations.

Note S5. Identification of the contact point

To precisely identify the position where the probe gets in contact with the sample, we used the protocol described in detail by Puricelli et al.[8]. δ_0 and α are left as free parameters while fitting the data. To find the contact point δ_0 of each force curve, the force curves are rescaled, linearised and a linear fit is performed over the first 10-15% of the indentation range[8]. δ_0 is the offset of indentation, which represents the point where a null force is exerted on the sample, thus it equals the point where the linear fit function intercepts the horizontal axis. The choice to fit the linearised Hertz model to the first 10-15% of the FC when a spherical indenter is used is supported by the observation that when $\gamma = \delta/R \leq 0.1$ (Figure 1b) the FCs simulated using parabolic and spherical indenters are in excellent agreement.

Eq.14 assumes that F^* does not depend on δ_0, which is strictly true when no corrections are applied; indeed, the functions Δ and Ω depend on δ_0 through the relation $\delta' = \delta + \delta_0$. In principle δ_0 could be considered as a free parameter to be determined through a nonlinear fit, which would cause the loss of the advantages of the linearisation. In practice, one can follow the procedure describe above for the case when no corrections are applied to determine a first estimate of δ_0 with good accuracy, then use Eqs. 14,16-18 with a new indentation axis shifted by δ_0, indicating a residual intercept $\Delta\delta_0$ in place of δ_0 in Eq. 14. Since $\Delta\delta_0$ is typically very small compared to the maximum indentation considered in the fit, neglecting it in the definition of the independent variable of the correction functions has no tangible effect.

Note S6. Mesh Optimization

The proximal region of the indenter-sample contact interface was finely meshed, while a coarser mesh was used moving away from it. Depending on the indentation range, elements as small as $0.026\ \mu m$ were used.

To optimise the mesh, we studied how the number of nodes affects the obtained Young's modulus E obtained through a Hertzian fit when a rigid sphere indents a sample sufficiently thick to avoid the bottom effect. Figure S6 shows that increasing the number of nodes above $N = 2 \cdot 10^4$ has a negligible impact on the value of the Young's modulus determined by extending the fit to increasingly wider ranges of indentation. Given that the computation time for carrying out a typical simulation on a desktop PC was below 60 minutes, we decided to use the maximum number of nodes allowed $N_{max} = 1.28 \cdot 10^5$ within a given mesh configuration.

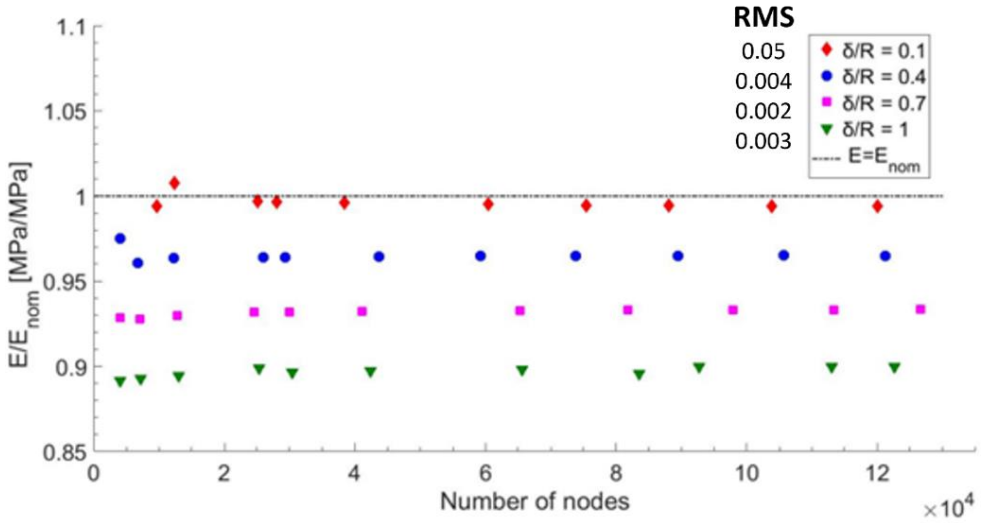

Figure S6. Impact of the number of nodes in the mesh of finite element simulations. The Young's modulus E was extracted by fitting the Hertz model to force curves simulated with the Bulk-Sphere (B-S) model, while $E_{\mathrm{nom}} = 0.5$ MPa is the nominal value used in the simulations. As the δ/R ratio increases and the contact departs from the hertzian model (large indentation effect), the Young's modulus decreases, irrespective of the number of nodes. The dashed line refers to the ideal hertzian contact. The root mean square (RMS) values of each series are reported.

Note S7. Preparation of the reference elastic sample

Following Refs[9–11], samples of *polyacrylamide* (IUPAC poly(2-propenamide), abbreviated in PA) were prepared. Polyacrylamide is a polymer created from *acrylamide* (A) monomers that bind to each other via free radicals provided by an *initiator* forming monomeric chains that, in turn, bind to each other in a process driven by a *cross linker* (B) agent.

Polyacrylamide is a suitable material to study the elastic properties of thin films because of its relative ease of preparation, the possibility to tune its Young's modulus of elasticity through a suitable proportioning between monomer and cross-linker[9,10], and because it maintains a linear elastic behaviour up to large deformations[12–14] (see also Gavara *et al.*[15]). The Young's modulus reflects the degree of structural organisation of the polymer at the level of molecular cross-linked chains, therefore changing the ratio monomer/cross-linker affects this organisation.

For the production of PA gels, we used acrylamide as the main component, bis-acrylamide (N,N*0*-Methylenebiscrylamide) as cross-linker and Irgacure 2959 as photoinitiator sensitive to UV light (wavelength 365 nm). Reagents were purchased from Sigma-Aldrich (St. Louis, MO). We prepared 50 mL of stock solution with concentrations of acrylamide $\rho_A = 0.12\ \mathrm{g/mL}$, *bis*-acrylamide $\rho_B = 0.0025\ \mathrm{g/mL}$ and photoinitiator $0.001\ \mathrm{g/mL}$ as follows: first, the proper amounts of acrylamide and bis-acrylamide were added to 50 mL of Milli-Q water and stirred for 30 minutes; then, the photoinitiator was added, the solution was covered to protect it from environmental light and was stirred for another 30 minutes. The solution was then poured into a 3D-printed moulds of desired shapes (see Figure S7), which were composed of lateral walls with no upper and lower covers. The bottom of the mould consisted of a glass slide pre-treated with plasma oxygen (Diener), while the top cover was a glass slide not treated with plasma. To polymerise, the samples were exposed to a 365 nm UV source[11]. After the polymerisation, the mould and the upper glass were removed and the samples were left swelling in Milli-Q water overnight, to reach the thermal and chemical equilibrium. All the tested samples were obtained from the same stock solution and moulds to ensure reproducibility.

Two types of PA samples were prepared, based on their thickness h, measured as the height with respect to the rigid glass substrate: bulk samples ($h \sim 1$ mm, Figure S7a), which are not affected by the bottom effect, and samples with a thickness gradient (Figure S7b), which can show the dependence of the extracted Young's modulus on the local thickness.

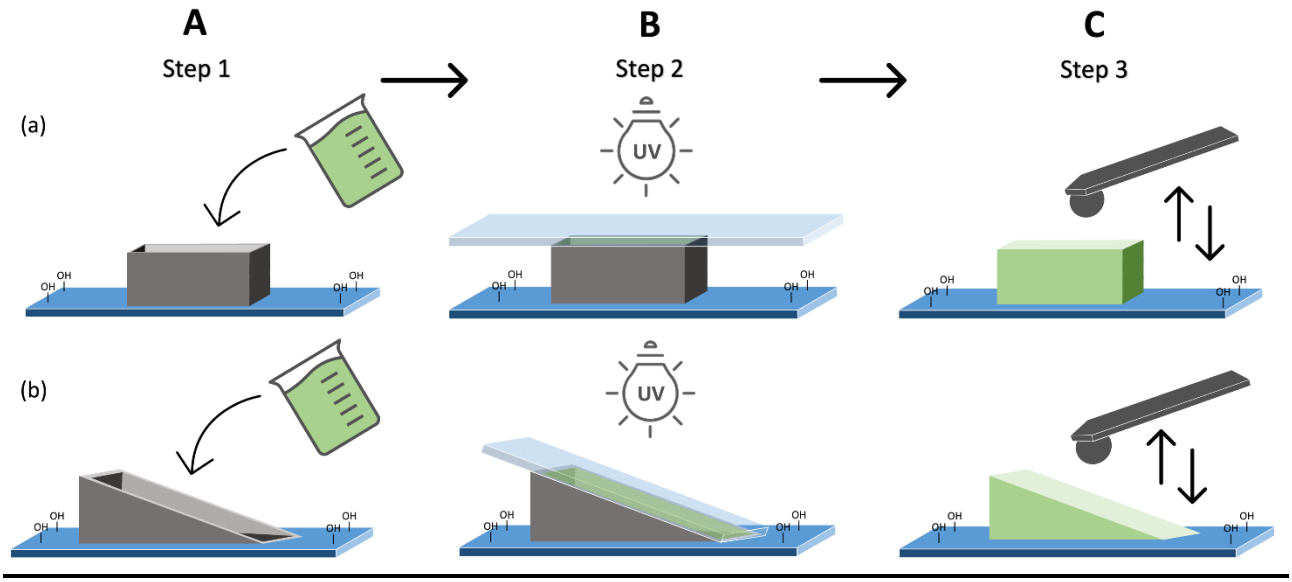

Figure S7. Representation of the elastic sample production. (**a**) *Bulk Sample*. A squared mould of height ≈ 1 mm closed by two glass slides is used. After the polymerisation of the poured solution, the upper coverslip and the mould are removed and then the gel was left to swell overnight in MilliQ water. The PA sample thickness is approximately 1 mm. (**b**) *Thickness-Gradient Sample.* A mould with variable height (maximum height 1 mm) and a 1 cm long edge is used (the inclination is 5.7°). After the polymerisation of the poured solution the upper coverslip and the mould are removed, and the swelling of the gel takes place. The sample possesses a linearly increasing thickness.

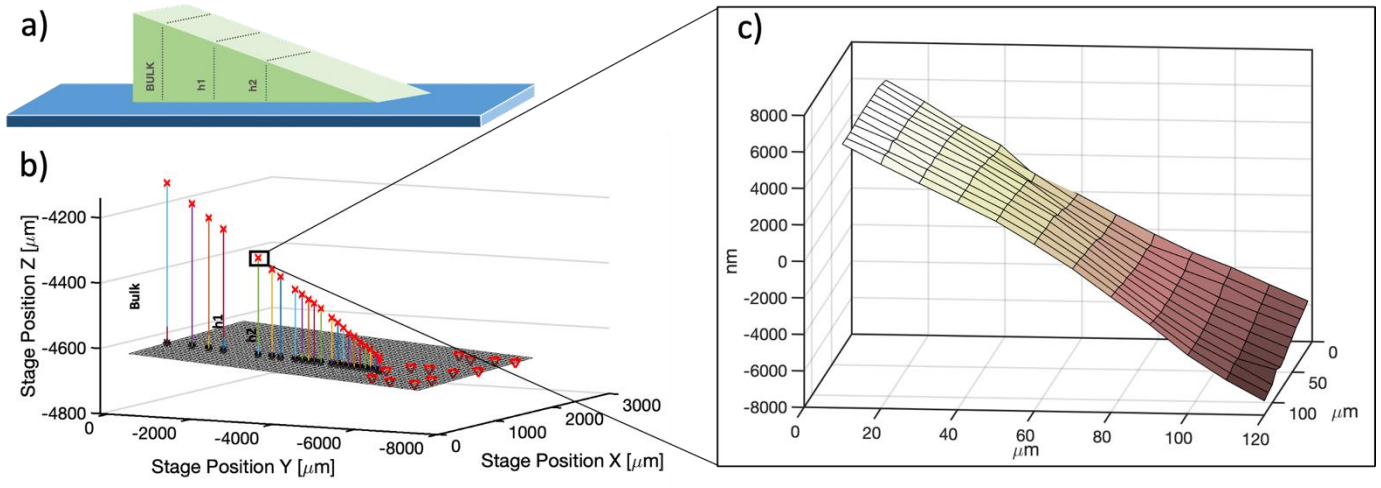

Figure S8. Local height measurement of the thickness gradient samples. (**a**) Schematic representation of the samples possessing a gradient of thickness *h* prepared according to the closed moulding process. (**b**) Experimental reconstruction of the sample height profile based on the measurement of local Z(X, Y) coordinates, using the z-microtranslator of the AFM head and the precision motorised micro-translation XY stage of the AFM, as described in the main text. (**c**) 3D plot representing the map of the local height variations around the mean thickness value of the FV, corresponding to the mean-subtracted contact point map, obtained from the FCs., reconstructed from the FCs.

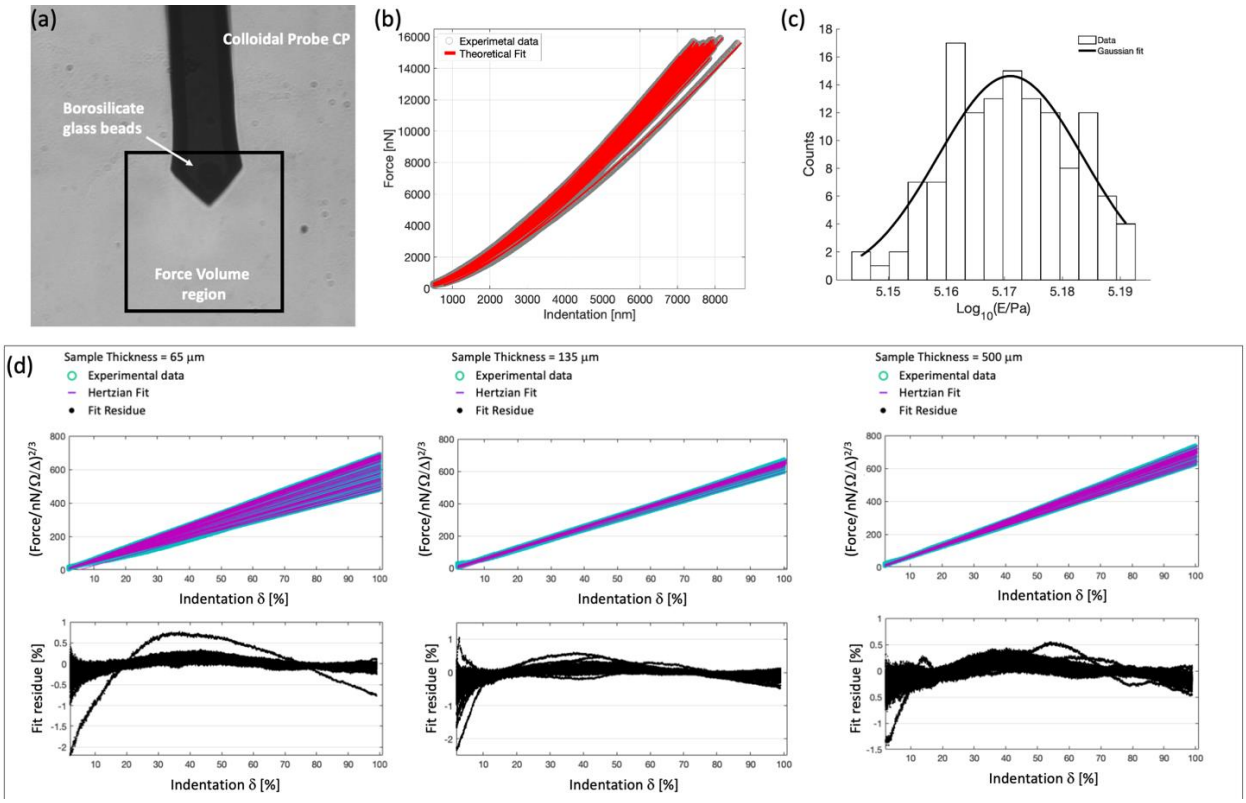

Figure S9. Schematics of the applied nanomechanical protocol. (a) Selection of the region of interest to acquire a Force Volume (FV) on the sample via optical microscopy. (b) Force curves extracted from the FV (already aligned and rescaled) with superimposed Hertzian fit. (c) Histogram of the Young's modulus values measured from each FC in semilog10 scale. The gaussian fit of the Young's modulus distribution in log scale provides the median Young's modulus value as: $E_{median}=10\log_{10}(E/Pa)|_{best}$, where $\log_{10}()|_{best}$ is the centre of the gaussian curve.(d) Three examples of linearized and corrected FCs fitted by the linearized hertz model, along with the fit residual plot.

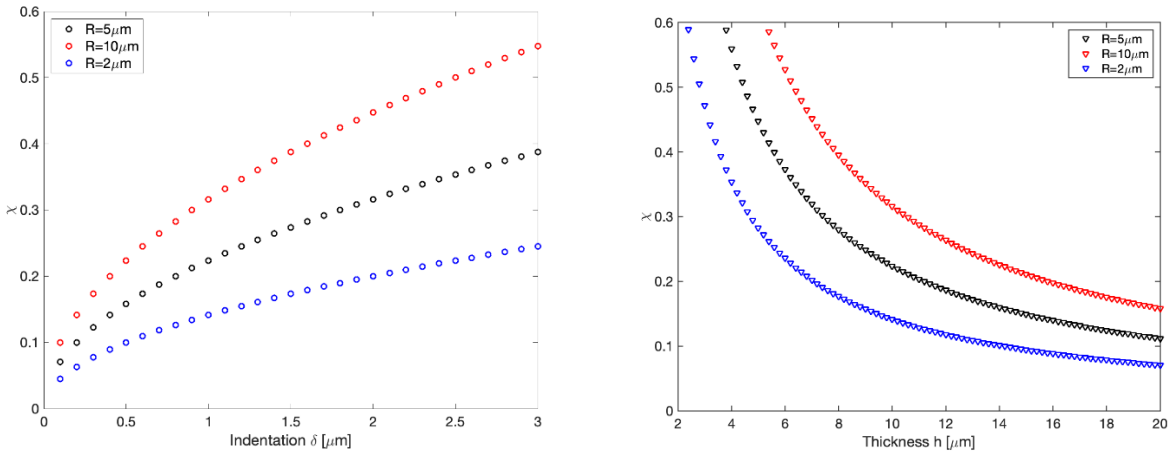

Figure S10. Dependence of χ from nanomechanical parameters. Dependence of χ on a) the indentation depth, and b) the sample thickness (δ = 1 µm), for different tip radii.

Note S8. Coupling between BEC and LIC

To elucidate the anomalous deviation at low χ in Figure 3f, we performed three simulations with medium thickness $h = 100$ μm, tip radii $R = 5,10,15$ μm and $\delta = R$ ($\gamma = 1$). In these conditions, $\chi < 0.15$ and $\chi\gamma$ is up to 0.14.

Figure S11a,b shows the relative discrepancy of the Young's modulus as a function of χ and $\chi\gamma$. It is evident that the discrepancy increases as the product $\chi\gamma$ increases, while χ remains below 0.15. When $\chi\gamma = 0.05$ the discrepancy is ~2%, in good agreement with the one observed in Figure 3f. When $\chi\gamma < 0.1$, the discrepancy is very small ($< 0.5\%$).

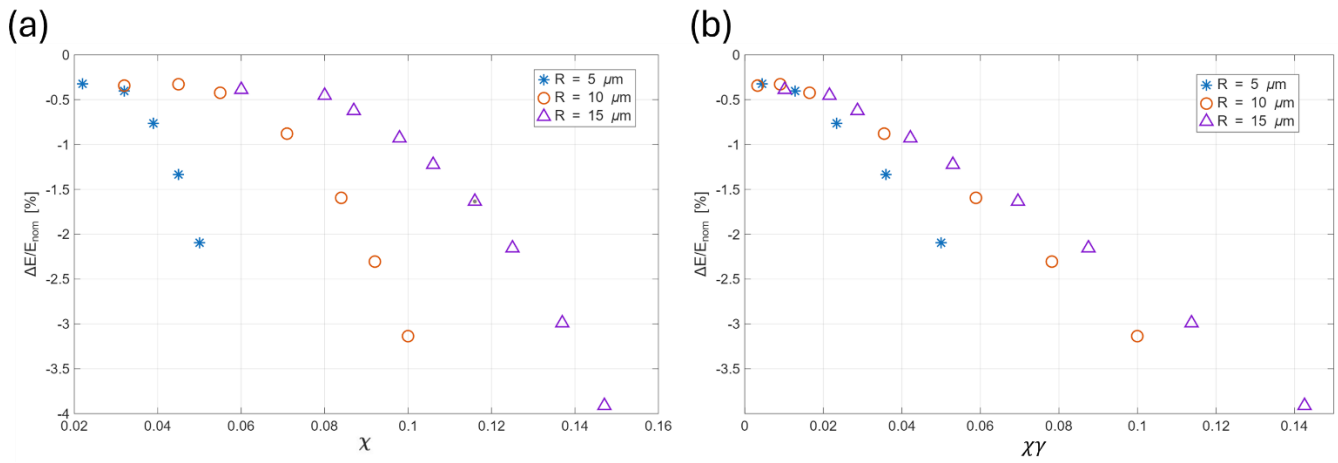

Figure S11. The impact of the $\chi\gamma$ factor on the accuracy of combined BEC_G and LIC_M. Relative discrepancy of the Young's modulus, after BEC_G+LIC_M, as a function of a) χ and b) $\chi\gamma$.

Note S9. Poroelasticity

The characteristic relaxation timescale τ_{poro} for poroelasticity scales as [16,17]:

$$\tau_{\mathrm{poro}} = \frac{a^2}{D} \tag{S16}$$

, where a is the contact radius and D is the diffusivity. For polyacrylamide gels, $D \sim 2 \cdot 10^2\ \mu\mathrm{m}^2/\mathrm{s}$.[16,18]

Any mechanical stimulus faster than τ_{poro} does not let water enough time to diffuse through the polymeric network, resulting in a stiffer elastic response due to water incompressibility[17].

In our experiments, δ increases up to a maximum value of several μm. The contact time τ_{contact} during loading in the bulk region is $\tau_{\mathrm{contact}} \approx 0.36\ \mathrm{s}$ for a ramp rate of 1 Hz. Considering a tip radius R = 8898 nm and a maximum indentation of 9 μm, and using Eq. S6 to calculate the contact radius, Eq. S6 predicts $\tau_{\mathrm{poro}} = 0.39\ \mathrm{s}$. Being τ_{poro} comparable to τ_{contact}, it is likely that poroelastic effects may be present, to some extent.

In the case of the thinnest region experimentally tested, $\tau_{\mathrm{contact}} \approx 0.21\ \mathrm{s}$ and the maximum indentation was 5.1 μm. If we assume that the spatial confinement does not affect the diffusivity D appreciably, the time constant τ_{poro} is 0.27 s.

Therefore, $\left(\tau_{\mathrm{contact}}/\tau_{\mathrm{poro}}\right)_{\mathrm{bulk}} \approx 0.92$ and for the thinnest region $\left(\tau_{\mathrm{contact}}/\tau_{\mathrm{poro}}\right)_{\mathrm{thin}} = 0.78$. The decreased ratio for the thinnest region points to the possibility that in our experiments, when the spatial confinement is more pronounced, the mechanical response is less influenced by the water displacement with respect to bulk regions, resulting in an apparent stiffening due to water incompressibility.

Moreover, it is known that spatially confined hydrogels exhibit a reduced diffusivity due to the presence of a rigid substrate which restraints the flow of water [17,19]. In addition, diffusivity would likely decrease if, as we argue, the crosslinking ratio and the material density increase in the thinner regions. If this is the case, we may expect an increase of τ_{poro} and a consequent stronger impact of poroelasticity, leading to a material stiffening. Whether the observed stiffening in the thinner region of the reference gel is dominated by the presumed increase of crosslinking ratio and material density (direct effect on material elasticity) or by the relaxation of the poroelastic timescale due to a reduced diffusivity of water through the polymeric network (indirect effect on material elasticity) it is hard to tell based on the available evidences.

Bibliography

1 S. V Kontomaris and A. Malamou, *Eur. J. Phys.*, 2021, **42**, 025010.

2 P. Müller, S. Abuhattum, S. Möllmert, E. Ulbricht, A. V. Taubenberger and J. Guck, *BMC Bioinformatics*, DOI:10.1186/s12859-019-3010-3.

3 W. C. Oliver and F. R. Brotzen, *J. Mater. Res.*, 1992, **7**, 613–617.

4 P. D. Garcia and R. Garcia, *Biophys. J.*, 2018, **114**, 2923–2932.

5 E. K. Dimitriadis, F. Horkay, J. Maresca, B. Kachar and R. S. Chadwick, *Biophys. J.*, 2002, **82**, 2798–2810.

6 D. C. Lin, D. I. Shreiber, E. K. Dimitriadis and F. Horkay, *Biomech. Model. Mechanobiol.*, 2009, **8**, 345–358.

7 S. R. Kalidindi and S. Pathak, *Acta Mater.*, 2008, **56**, 3523–3532.

8 L. Puricelli, M. Galluzzi, C. Schulte, A. Podestà and P. Milani, *Review of Scientific Instruments*, 2015, **86**, 33705.

9 J. R. Tse and A. J. Engler, *Curr. Protoc. Cell Biol.*, DOI:10.1002/0471143030.cb1016s47.

10 A. K. Denisin and B. L. Pruitt, *ACS Appl. Mater. Interfaces*, 2016, **8**, 21893–21902.

11 S. Sheth, E. Jain, A. Karadaghy, S. Syed, H. Stevenson and S. P. Zustiak, *Int. J. Polym. Sci.*, DOI:10.1155/2017/5147482.

12 Z. Cao, Z. Yuan, R. Wu, H. Wu, B. Jin, J. Zheng and J. Wu, *Gels*, 2021, **7**, 177.

13 C. Storm, J. J. Pastore, F. C. MacKintosh, T. C. Lubensky and P. A. Janmey, *Nature*, 2005, **435**, 191–194.

14 A. Engler, L. Bacakova, C. Newman, A. Hategan, M. Griffin and D. Discher, *Biophys. J.*, 2004, **86**, 617–628.

15 N. Gavara and R. S. Chadwick, *Nat. Nanotechnol.*, 2012, **7**, 733–736.

16 P. C. Nalam, N. N. Gosvami, M. A. Caporizzo, R. J. Composto and R. W. Carpick, *Soft Matter*, 2015, **11**, 8165–8178.

17 D. Xu, M. L. Hernandez Miranda, N. D. Evans, B. G. Sengers, M. Browne and R. B. Cook, *J. Mech. Behav. Biomed. Mater.*, DOI:10.1016/j.jmbbm.2023.106195.

18 Z. I. Kalcioglu, R. Mahmoodian, Y. Hu, Z. Suo and K. J. Van Vliet, *Soft Matter*, 2012, **8**, 3393–3398.

19 E. P. Chan, Y. Hu, P. M. Johnson, Z. Suo and C. M. Stafford, *Soft Matter*, 2012, **8**, 1492–1498.